ENFORCING HARD PHYSICAL CONSTRAINTS IN CNNS THROUGH DIFFERENTIABLE PDE LAYER

Chiyu "Max" Jiang
UC Berkeley
chiyu.jiang@berkeley.edu

Karthik Kashinath
Lawrence Berkeley National Lab
kkashinath@lbl.gov

Prabhat
Lawrence Berkeley National Lab
prabhat@lbl.gov

Philip Marcus
UC Berkeley
pmarcus@me.berkeley.edu

ABSTRACT

Recent studies at the intersection of physics and deep learning have illustrated successes in the application of deep neural networks to partially or fully replace costly physics simulations. Enforcing physical constraints to solutions generated by neural networks remains a challenge, yet it is essential to the accuracy and trustworthiness of such model predictions. Many systems in the physical sciences are governed by Partial Differential Equations (PDEs). Enforcing these as hard constraints, we show, are inefficient in conventional frameworks due to the high dimensionality of the generated fields. To this end, we propose the use of a novel differentiable spectral projection layer for neural networks that efficiently enforces spatial PDE constraints using spectral methods, yet is fully differentiable, allowing for its use as a layer within Convolutional Neural Networks (CNNs) during end-to-end training. We show that its computational cost is cheaper than a single convolution layer. We apply it to an important class of physical systems - incompressible turbulent flows, where the divergence-free PDE constraint is required. We train a 3D Conditional Generative Adversarial Network (CGAN) for turbulent flow superresolution efficiently, while guaranteeing the spatial PDE constraint of zero divergence. Furthermore, our empirical results show that the model produces realistic flow statistics when trained with hard constraints imposed via the proposed novel differentiable spectral projection layer, as compared to soft constrained and unconstrained counterparts.

1 INTRODUCTION

Convolutional Neural Network (CNN) based deep learning architectures have achieved huge success in many tasks across computer vision, but their use in the physical sciences, and in particular fluid dynamics (Tompson et al. (2017); Xie et al. (2018); Kim et al. (2018)), have only recently been explored. Unlike computer vision problems, physical fields are often constrained by PDEs that arise from the governing equations of the physical system. For example, the Poisson equation of the form $\nabla^2\phi = f$ is often encountered in heat diffusion problems, whereas the divergence-free (also known as solenoidal) conditions in the form of $\nabla \cdot \boldsymbol{\phi} = 0$ is fundamental to magnetic fields, as well as incompressible fluid velocity fields to ensure conservation of mass. For meaningful application of deep learning to a range of important physical problems, it is essential to enforce such spatial PDE constraints to guarantee physical consistency and reliability of the model output for scientific applications. Yet, general means of enforcing these constraints do not exist and the existing methods (Salzmann & Urtasun (2010); Varol et al. (2012); Pathak et al. (2015); Márquez-Neila et al. (2017); Amos & Kolter (2017); Frerix et al. (2019)) do not scale well with high dimensional, high resolution outputs. Other works that incorporate physical constraints in neural networks utilize soft constraints with fully connected networks (Raissi (2018); Raissi et al. (2018; 2019)) and do not levarage the spatial efficiencies of CNNs.

In this paper, we address this issue by proposing a novel differentiable PDE layer (PDEL) that efficiently enforces spatial PDE constraints for neural networks within CNNs, at costs on par with *a single CNN layer*. We use spectral methods, which leverages the highly efficient Fast Fourier Transform (FFT) algorithm for enforcing such constraints. Using this formulation, we are able to exploit the structures of the spectral matrices corresponding to these differential operators that renders the entire layer $\mathcal{O}(n \log n)$ for processing a 3 dimensional field of size n. The method is general for enforcing arbitrary linear combinations of differential operators on these fields, which encompasses physical constraints from a broad range of important scientific and engineering systems. We apply this hard constraining layer to the problem of turbulence superresolution, where we show that training with the hard constraining layer in-the-loop not only guarantees that the imposed constraint is strictly satisfied, but also generates solutions that are more accurate measured via a variety of fluid flow metrics.

2 METHODS

We present a novel method for efficiently enforcing hard linear spatial PDE constraints within CNNs using spectral methods (Canuto et al. (1988)). This is in the context of underdetermined systems, since solutions do not exist for overdetermined systems, while solutions for determined systems do not fit in the context of constraining the outputs. More specifically, given the output of the network to be a discretization of a 3D vector field $\boldsymbol{f} : \mathbb{R}^3 \mapsto \mathbb{R}^3$ and a linear spatial PDE operator $A((\frac{\partial}{\partial x_j})^0, (\frac{\partial}{\partial x_j})^1, \cdots)$ that maps vector fields to scalar fields $A\boldsymbol{f} : \mathbb{R}^3 \mapsto \mathbb{R}$, we seek a means of efficiently imposing the spatial linear PDE constraints within CNNs, i.e.,

$$A\boldsymbol{f} = \boldsymbol{b} \tag{1}$$

Note that this form encompasses a wide range of physically relevant constraints. In particular, all spatial PDE constraints composed of divergence, curl, Laplacian and other higher order partial differential terms in linear combination may be expressed in this form. Depending on the domain of application, this includes mass conservation for incompressible fluid flows, the heat equation, the wave equation, Laplace's equation, Helmholtz equation, Klein-Gordon equation, and Poisson equation. For the important constraint of mass conservation in incompressible flows, we investigate the divergence-free (solenoidal) constraint of:

$$\nabla \cdot \boldsymbol{f} = \sum_j \frac{\partial}{\partial x_j} \boldsymbol{f}_j = \boldsymbol{0} \tag{2}$$

We present our main results for computing the spectral projection operator that efficiently enforces the solenoidal condition using spectral methods. We defer readers to Eqns (14 - 27) of Appendix C for detailed derivation of these results. In spectral space, the projection of the original vector field $\boldsymbol{F}$ into solution space: $\hat{\boldsymbol{F}}$, can be computed by:

$$\hat{\boldsymbol{F}} = P\boldsymbol{F} + Q\boldsymbol{B} \tag{3}$$

$$P = I - \frac{1}{\sum_{j=0}^{3} A_j^2} \begin{bmatrix} A_1^2 & A_1 A_2 & A_1 A_3 \\ A_1 A_2 & A_2^2 & A_2 A_3 \\ A_1 A_3 & A_2 A_3 & A_3^2 \end{bmatrix} ; Q = -\frac{1}{\sum_{j=0}^{3} A_j^2} \begin{bmatrix} A_1 \\ A_2 \\ A_3 \end{bmatrix} \tag{4}$$

where $\boldsymbol{F} = \text{FFT}(\boldsymbol{f}), \boldsymbol{B} = \text{FFT}(\boldsymbol{b})$ with FFT denoting the Fast Fourier Transform operator, and A_i denoting the i-th component of the spectral gradient operator.

3 EXPERIMENTS AND RESULTS

3.1 COMPUTATIONAL COMPLEXITY AND COST

We first show that although the classic Lagrangian based hard constraining method is general and able to enforce hard linear constraints, solving it by direct inversion leads to poor computational efficiency, especially with high-resolution 3-dimensional data outputs from CNNs. Each linear projection step solved by direct inversion is of complexity $\mathcal{O}((3n)^2) \sim \mathcal{O}(9n^2)$ operations. In comparison, the spectral projection method only involves element-wise operations, resulting in an overall complexity of $\mathcal{O}(n)$ operations for enforcing constraints, and $\mathcal{O}(n \log(n))$ for the FFT and IFFT operations. Results of an empirical analysis for computational time and memory usage is shown in Fig. 1.

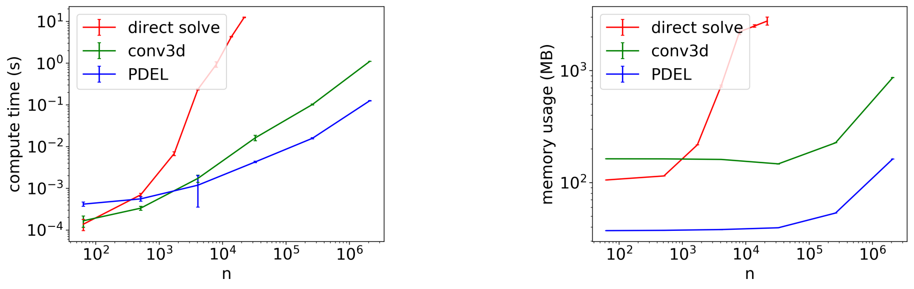

(a) Compute time vs system size

(b) Peak memory usage vs system size

Figure 1: Comparison of computational performance for direct solve using Lagrangian multiplier method and our PDE Layer (PDEL). Computational performance for a single Conv3d layer of kernel size 3 is also included for comparison purposes. Our PDEL fairs well with respect to size of the linear system, even compared with the highly optimized 3D convolution layers, allowing for its direct integration into CNN architectures. Direct solve leads to memory overflow at very small output resolutions (24^3). Above computation benchmarks performed on a 2.4 GHz CPU chip.

3.2 Turbulence Superresolution with Conditional GAN

Problem setup The main target application of this study is the super-resolution of turbulent flow fields. Fully resolving turbulence requires direct numerical simulation (DNS) that can resolve the smallest scales of the flow (Komogorov scale), which is prohibitively expensive. Therefore, the motivation of this study is to produce flow fields and flow statistics comparable to DNS at the cost of a low-resolution proxy, while strictly enforcing PDE constraints. To this end, we leverage high-resolution DNS data to train a deep neural network to learn the mapping between the low-resolution flow and its high-resolution counterpart. We compare between several algorithms for the task: the conventional trilinear interpolation which is not learning based, and various variations of the GauGAN architecture (Park et al. (2019)) for conditional generative modeling. The compared methods for enforcing PDE constraints are below: (1) GauGAN with our PDE Layer inserted as a last layer after the generator to enforce hard PDE constraints (2) GauGAN with soft PDE constraint as an additional loss term, and (3) no PDE constraints. Furthermore, since PDEL layer can be utilized either only at test time or both at test time and also used in-the-loop during training, we investigate the use of PDEL during training time to see how it improves the model effectiveness. We use the Forced Isotropic Turbulence dataset from the Johns Hopkins Turbulence Database for this experiment (Perlman et al. (2007)).

Evaluation metrics we refrain from directly comparing the norm of the difference in velocity fields, as turbulence solutions are chaotic. Instead, we compare the distributions of various key flow statistics, as outlined by Perlman et al. (2007), which are more informative from a turbulence modeling standpoint. The flow statistics in Tab. 1 is defined as below. For simplicity, we denote the different velocity components using Einstein notation, and use angle brackets <> to denote spatial averaging.

- Total kinetic energy, $E_{\text{tot}} = \frac{1}{2} < u_i u_i >$
- Dissipation, $\epsilon = 2\nu < \sigma_{ij}\sigma_{ij} >$, where $\sigma_{ij} := \frac{1}{2}\left(\frac{\partial u_i}{\partial x_j} + \frac{\partial u_j}{\partial x_i}\right)$, and $\nu = 0.000185$ is a constant for fluid viscosity.
- Large eddy turnover time: $T_L = L/u'$, where $L = \frac{\pi}{2u'^2}\int \frac{E(k)}{k}dk$ and $u' = \sqrt{(2/3)E_{\text{tot}}}$

Results The main quantitative results for this experiment are presented in Tab. 1, whereas a visualization of the distributions regarding various key flow statistics are presented in Fig. 2. Results indicate that while soft constraining can encourage the network to adhere to constraints, its residue is nonzero, implying that the imposed constraint is not strictly satisfied. Spectral based projection method can effectively eliminate residue. Training with the PDE layer in-the-loop eliminates residue and achieves greater accuracy on key statistical quantities, as compared to unconstrained and soft constrained cases, even when hard constraints are enforced at test time. We note that although this

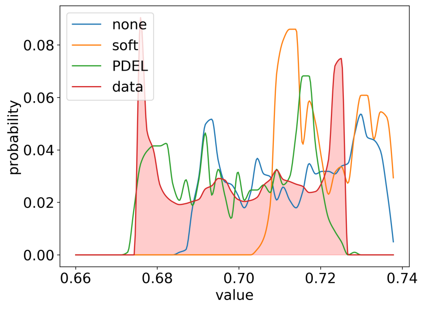

(a) Turbulent Kinetic Energy

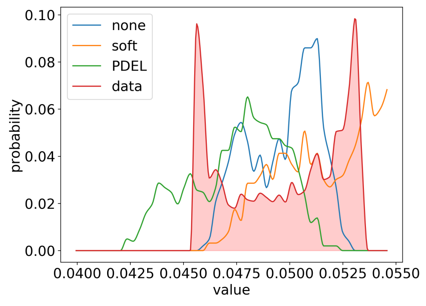

(b) Dissipation

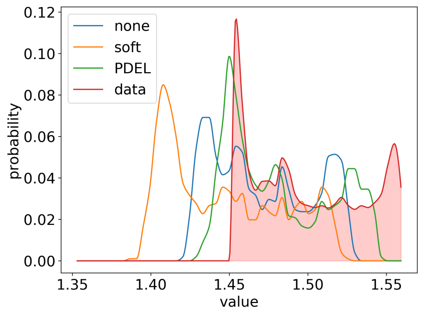

(c) Large Eddy Turnover Time

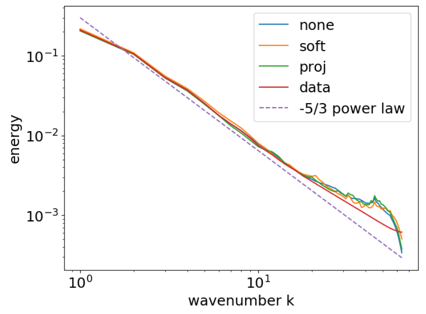

(d) Spectrum Plot

Figure 2: Probability Density Function plots of samples generated by various models as well as ground truth distributions (highlighted in red). The quality of the distributions compared against the ground truth distributions are captured well by the KS statistic and mean difference measurements in Tab. 1. (d) Shows the spectrum, where all methods trail the data distribution well in the low wavenumber regime and deviate at higher wavenumbers.

Constraint Type		No PDE Layer			PDEL at test time			In-the-loop
		Trilinear	None	Soft	Trilinear	None	Soft	PDEL
Residue(↓)		3.597	19.763	0.150	**0.000**	**0.000**	**0.000**	**0.000**
KS Stats (↓)	tkenergy	1.000	0.308	0.712	1.000	0.216	0.632	0.163
	dissipation	1.000	0.283	0.549	1.000	1.000	0.332	0.422
	eddytime	1.000	0.388	0.599	1.000	0.229	0.487	0.276
	mean	1.000	0.326	0.620	1.000	0.482	0.484	**0.287**
Mean Diff (↓)	tkenergy	6.227	0.745	2.192	6.593	0.396	1.845	0.106
	dissipation	16.245	0.016	1.301	16.732	2.690	0.731	0.804
	eddytime	9.343	0.878	1.516	10.037	0.436	1.125	0.591
	mean	10.605	0.546	1.670	11.121	1.174	1.234	**0.500**

Table 1: Comparison of generated distributions on test set against ground truth distribution on test set. Smaller values indicate a better match between distributions.

method is not the most accurate for the dissipation statistic, presumably because of discrepancies in the high wavenumber regime (where dissipation occurs), the overall mean statistics and individual statistics for the other metrics are superior compared to all the other compared methods.

4 Conclusions and Future Work

Enforcing hard physical constraints to solutions generated using neural networks are essential for their application to important scientific problems. Some key limitations of this work are: (i) the method is applicable in its current form only to flows with periodic boundary conditions; (ii) we only develop a method for linear spatial constraints and (iii) we only consider statistically steady flows. In future we will address all the above limitations to extend our work to more general sets of nonlinear unsteady constraints with arbitrary boundary conditions.

REFERENCES

Brandon Amos and J Zico Kolter. Optnet: Differentiable optimization as a layer in neural networks. In *Proceedings of the 34th International Conference on Machine Learning-Volume 70*, pp. 136–145. JMLR. org, 2017.

Claudio Canuto, M. Yousuff Hussaini, Alfio Quarteroni, and Thomas A. Zang. *Spectral Methods in Fluid Dynamics*. Springer Berlin Heidelberg, 1988. doi: 10.1007/978-3-642-84108-8. URL `https://doi.org/10.1007/978-3-642-84108-8`.

Thomas Frerix, Daniel Cremers, and Matthias Nießner. Linear inequality constraints for neural network activations. *arXiv preprint arXiv:1902.01785*, 2019.

Byungsoo Kim, Vinicius C. Azevedo, Nils Thuerey, Theodore Kim, Markus H. Gross, and Barbara Solenthaler. Deep fluids: A generative network for parameterized fluid simulations. *CoRR*, abs/1806.02071, 2018. URL `http://arxiv.org/abs/1806.02071`.

Pablo Márquez-Neila, Mathieu Salzmann, and Pascal Fua. Imposing hard constraints on deep networks: Promises and limitations. *arXiv preprint arXiv:1706.02025*, 2017.

Taesung Park, Ming-Yu Liu, Ting-Chun Wang, and Jun-Yan Zhu. Semantic image synthesis with spatially-adaptive normalization. *arXiv preprint arXiv:1903.07291*, 2019.

Deepak Pathak, Philipp Krahenbuhl, and Trevor Darrell. Constrained convolutional neural networks for weakly supervised segmentation. In *Proceedings of the IEEE international conference on computer vision*, pp. 1796–1804, 2015.

E. Perlman, R. Burns, Y. Li, and C. Meneveau. Data exploration of turbulence simulations using a database cluster. In *SC '07: Proceedings of the 2007 ACM/IEEE Conference on Supercomputing*, pp. 1–11, Nov 2007. doi: 10.1145/1362622.1362654.

Maziar Raissi. Deep hidden physics models: Deep learning of nonlinear partial differential equations. *arXiv preprint arXiv:1801.06637*, 2018.

Maziar Raissi, Alireza Yazdani, and George Em Karniadakis. Hidden fluid mechanics: A navier-stokes informed deep learning framework for assimilating flow visualization data. *arXiv preprint arXiv:1808.04327*, 2018.

Maziar Raissi, Paris Perdikaris, and George E Karniadakis. Physics-informed neural networks: A deep learning framework for solving forward and inverse problems involving nonlinear partial differential equations. *Journal of Computational Physics*, 378:686–707, 2019.

Mathieu Salzmann and Raquel Urtasun. Implicitly constrained gaussian process regression for monocular non-rigid pose estimation. In *Advances in Neural Information Processing Systems*, pp. 2065–2073, 2010.

Jonathan Tompson, Kristofer Schlachter, Pablo Sprechmann, and Ken Perlin. Accelerating Eulerian fluid simulation with convolutional networks. In Doina Precup and Yee Whye Teh (eds.), *Proceedings of the 34th International Conference on Machine Learning*, volume 70 of *Proceedings of Machine Learning Research*, pp. 3424–3433, International Convention Centre, Sydney, Australia, 06–11 Aug 2017. PMLR. URL `http://proceedings.mlr.press/v70/tompson17a.html`.

Aydin Varol, Mathieu Salzmann, Pascal Fua, and Raquel Urtasun. A constrained latent variable model. In *2012 IEEE Conference on Computer Vision and Pattern Recognition*, pp. 2248–2255. Ieee, 2012.

You Xie, Erik Franz, Mengyu Chu, and Nils Thuerey. tempoGAN: A Temporally Coherent, Volumetric GAN for Super-resolution Fluid Flow. *arXiv e-prints*, art. arXiv:1801.09710, Jan 2018.

APPENDIX

A ENFORCING LINEAR CONSTRAINTS

We first discuss enforcing linear constraints on the outputs of the neural network, where we have a neural network that learns the function mapping $f : \mathbb{R}^t \mapsto \mathbb{R}^m$, where the function $f(\boldsymbol{x}; \boldsymbol{\theta})$ is parameterized by learnable parameters $\boldsymbol{\theta}$, and is subject to the linear constraint $Af(\boldsymbol{x}; \boldsymbol{\theta}) = \boldsymbol{b}$, where $A \in \mathbb{R}^{n\times m}, \boldsymbol{b} \in \mathbb{R}^n$. For this to be an underconstrained system, we have $n < m$. Two forms of constraints are possible for explicitly enforcing a certain set of constraints for neural network outputs: soft constraints and hard constraints.

Soft constraints are easy to implement, by adding a differentiable residual loss for penalizing the network during training time for violating the explicit constraints. For simplicity, let $\boldsymbol{y} := f(\boldsymbol{x}; \boldsymbol{\theta})$. In the conventional unconstrained case, assume the neural network is trained under the differentiable loss function $L(f(\boldsymbol{x}; \boldsymbol{\theta}))$, in the constrained case, the loss function can be augmented by an additional residual loss term defined by:

$$L_c(\theta) = L(\theta) + \alpha((A\boldsymbol{y} - b)^T(A\boldsymbol{y} - b)) \tag{5}$$

where α is a hyper-parameter weighing the two loss functions that can be difficult to determine and vary between applications. Although easy to implement, soft constraints provide no guarantees on the solutions satisfying the imposed constraint.

Hard linear constraints can be enforced by posing the problem as a constrained optimization problem for seeking the closest point in the solution space subject to the constraints, which can be solved by satisfying the Karush-Kuhn-Tucker (KKT) condition. The result of the projection step can be written as the stationary point of the Lagrangian:

$$\min_{\hat{\boldsymbol{y}}} \max_{\boldsymbol{\lambda}} \mathcal{L}(\hat{\boldsymbol{y}}, \boldsymbol{\lambda}) \tag{6}$$

where we have the Lagrangian as:

$$\mathcal{L}(\hat{\boldsymbol{y}}, \boldsymbol{\lambda}; \boldsymbol{y}) = \frac{1}{2}(\boldsymbol{y} - \hat{\boldsymbol{y}})^T(\boldsymbol{y} - \hat{\boldsymbol{y}}) + \boldsymbol{\lambda}^T(A\boldsymbol{y} - \boldsymbol{b}) \tag{7}$$

$$\frac{\partial \mathcal{L}}{\partial \hat{\boldsymbol{y}}} = \boldsymbol{y} - \hat{\boldsymbol{y}} + \boldsymbol{\lambda}^T A \tag{8}$$

The KKT condition leads to the following linear system, the solution of which involves solving a linear system of dimensions $(m + n) \times (m + n)$. Given that the linear system is symmetric and positive definite, the solution can be sought by inverting the system:

$$\begin{bmatrix} I & A^T \\ A & 0 \end{bmatrix} \begin{bmatrix} \hat{\boldsymbol{y}} \\ \boldsymbol{\lambda} \end{bmatrix} = \begin{bmatrix} \boldsymbol{y} \\ \boldsymbol{b} \end{bmatrix} \Rightarrow \begin{bmatrix} \hat{\boldsymbol{y}} \\ \boldsymbol{\lambda} \end{bmatrix} = \begin{bmatrix} I & A^T \\ A & 0 \end{bmatrix}^{-1} \begin{bmatrix} \boldsymbol{y} \\ \boldsymbol{b} \end{bmatrix} \tag{9}$$

While this approach is general for enforcing arbitrary linear constraints on arbitrary network outputs, it is difficult to scale it to higher dimensions, and particularly difficult for 2-dimensional and 3-dimensional outputs, by direct matrix inversion followed by matrix multiplication.

B SPECTRAL METHODS

We present an overview of the spectral methods (Canuto et al. (1988)) for discretizing the spatial PDE operators. Spectral methods are a class of numerical methods that computes the spatial partial derivatives of a field based on the spectral decomposition of the signal. By decomposing the original signal into a linear combination with respect to trigonometric basis functions of varying wavenumbers (or frequencies), the spatial derivatives with respect to the trigonometric basis functions can be easily and efficiently computed. The Fast Fourier Transform (FFT) is a well known algorithm for efficiently computing the Direct Fourier Transform (DFT) of uniform discrete signals. The multidimensional FFT and inverse FFT respectively compute the following:

$$\boldsymbol{F}^{(\boldsymbol{k})} = \sum_{\boldsymbol{n}=0}^{\boldsymbol{N}-1} \boldsymbol{f}^{(\boldsymbol{n})} e^{-i2\pi \boldsymbol{k}\cdot(\boldsymbol{n}/\boldsymbol{N})};\ \boldsymbol{f}^{(\boldsymbol{n})} = \frac{1}{N_1 N_2 N_3} \sum_{\boldsymbol{k}=0}^{\boldsymbol{N}-1} \boldsymbol{F}^{(\boldsymbol{k})} e^{i2\pi \boldsymbol{k}\cdot(\boldsymbol{n}/\boldsymbol{N})} \tag{10}$$

where $\boldsymbol{F}^{(\boldsymbol{k})} = \text{FFT}(\boldsymbol{f}^{(\boldsymbol{n})}), \boldsymbol{f}^{(\boldsymbol{n})} = \text{IFFT}(\boldsymbol{F}^{(\boldsymbol{k})})$, spatial indices $\boldsymbol{n} = (n_1, n_2, n_3), n_j \in \{0, 1, \cdots, N_j - 1\}$ and spectral indices $\boldsymbol{k} = (k_1, k_2, k_3), k_j \in \{0, 1, \cdots, N_j - 1\}$. The spatial derivative with respect to x_j can be computed by:

$$\frac{\partial}{\partial x_j} \boldsymbol{f}^{(\boldsymbol{n})} = \text{IFFT}(ik_j \boldsymbol{F}^{(\boldsymbol{k})}) \tag{11}$$

In matrix form, for the t-th component of a 3 dimensional vector field: $\boldsymbol{F}_t$, taking its flattened vector form, and taking the flattened vector form of the wavenumber $\boldsymbol{k}_j$ corresponding to the dimension x_j, the spatial derivative with respect to x_j can be computed using matrix multiplication:

$$\frac{\partial}{\partial x_j} \boldsymbol{F}_t = diag(i\boldsymbol{k}_j)\boldsymbol{F}_t \tag{12}$$

where $diag()$ converts a vector into a corresponding diagonal matrix. In general, arbitrary linear combination of spatial derivatives of varying orders can be computed using a single diagonal matrix multiplication:

$$(\sum_j \sum_r c_{jr} \Big(\frac{\partial}{\partial x_j}\Big)^r)\boldsymbol{F}_t = diag(\sum_j \sum_r c_{jr}(i\boldsymbol{k}_j)^r)\boldsymbol{F}_t := A_t \boldsymbol{F}_t \tag{13}$$

where A_t is a diagonal matrix for the spatial derivatives corresponding to the t-th component of the vector field, that is a polynomial of $i\boldsymbol{k}_j$, and $A = [A_1, A_2, A_3]$.

C Mathematical Derivation for Spectral Projection

The solution to the Lagrangian multiplier method for enforcing the solenoidal conditions involves inverting the left-hand-side matrix in Eqn. 9. Since $I, A, 0$ are block matrices, the inverse can be represened by

$$\begin{bmatrix} I & A^T \\ A & 0 \end{bmatrix}^{-1} = \begin{bmatrix} I - A^T(AA^T)^{-1}A & A^T(AA^T)^{-1} \\ (AA^T)^{-1}A & -(AA^T)^{-1} \end{bmatrix} \tag{14}$$

Hence the projected vector in spectral space can be computed as:

$$\hat{\boldsymbol{F}} = P\boldsymbol{F} + Q\boldsymbol{B} \tag{15}$$

The second term in the equation above drops out since $\boldsymbol{b} = 0$ for solenoidal constraints. More specifically for spectral methods, the matrix A can be represented as three diagonal matrices for the wavenumbers in the three dimensions multiplied by the imaginary number i:

$$A = \begin{bmatrix} \ddots & & \ddots & & \ddots & \\ & A_1 & & A_2 & & A_3 \\ & & \ddots & & \ddots & & \ddots \end{bmatrix} \tag{16}$$

$$= [A_1 \quad A_2 \quad A_3] \tag{17}$$

The only matrix inverse associated is AA^T, whose value can be computed by block matrix multiplication:

$$AA^T = A_1^2 + A_2^2 + A_3^2 \tag{18}$$

Given that A_1, A_2, A_3 are diagonal matrices (eliminating the terms regarding the $[0, 0, 0]$ mode), its inverse can be computed by directly inverting the diagonal terms:

$$(AA^T)^{-1} = \frac{1}{A_1^2 + A_2^2 + A_3^2} \tag{19}$$

Hence the linear projection matrix can be written as:

$$I - A^T(AA^T)^{-1}A = I - \frac{1}{A_1^2 + A_2^2 + A_3^2} \begin{bmatrix} A_1^2 & A_1A_2 & A_1A_3 \\ A_1A_2 & A_2^2 & A_2A_3 \\ A_1A_3 & A_2A_3 & A_3^2 \end{bmatrix} \tag{20}$$

$$A^T(AA^T)^{-1} = -\frac{1}{\sum_{j=0}^{3} A_j^2} \begin{bmatrix} A_1 \\ A_2 \\ A_3 \end{bmatrix} \tag{21}$$

Notation	Description
Conv(n)	3D convolution block with n output layers
SResBlock	SPADE Residue Block consisting of SPADE + ReLU + Conv + SPADE + ReLU + Conv
Up(n)	Upsampling layer with nearest neighbor interpolation with scaling factor of n
IN	3D Instance Normalization Layer

Table 2: Description of module notations in Fig. 3

Recovering the same solution as in Eqn. 4. More specifically for the divergence-free condition, we have:

$$A_j = diag(-i\boldsymbol{k}_j) \tag{22}$$

$$\boldsymbol{B} = \boldsymbol{0} \tag{23}$$

Hence the spectral projection step can be further simplified as:

$$\hat{\boldsymbol{F}} = \boldsymbol{F} - \frac{\boldsymbol{k} \cdot \boldsymbol{F}}{\boldsymbol{k} \cdot \boldsymbol{k}} \boldsymbol{k} \tag{24}$$

It is easy to show that the result is divergence-free, since:

$$-i\boldsymbol{k}\hat{\boldsymbol{F}} = -i\boldsymbol{k}\boldsymbol{F} + i\boldsymbol{k}\boldsymbol{F} = \boldsymbol{0} \tag{25}$$

It is also easy to show that the projection is orthogonal to the solution space, since the dot product between the $\hat{\boldsymbol{F}} - \boldsymbol{F}$ and $\hat{\boldsymbol{F}}$ is zero:

$$(\hat{\boldsymbol{F}} - \boldsymbol{F}) \cdot \hat{\boldsymbol{F}} = -(\frac{\boldsymbol{k} \cdot \boldsymbol{F}}{\boldsymbol{k} \cdot \boldsymbol{k}}\boldsymbol{k}) \cdot (\boldsymbol{F} - \frac{\boldsymbol{k} \cdot \boldsymbol{F}}{\boldsymbol{k} \cdot \boldsymbol{k}}\boldsymbol{k}) \tag{26}$$

$$= \boldsymbol{0} \tag{27}$$

D MODEL AND TRAINING DETAILS

We use the GauGAN architecture (with schematics as shown in Fig. 3) for the conditional flow field generation task. The abbreviated names for the various modules are given in Tab. 2. Our model differs from the original GauGAN model in two distinct aspects. First, our architecture utilizes 3 dimensional convolutions instead of the 2 dimensional counterparts in the original GauGAN architecture. Second, for our hard constrained case, we append the spectral projection layer to the end of the architecture for enforcing hard constraints.

For training the model, we use multiresolution discriminator loss as in Park et al. (2019) across 3 discriminators. We train the model with batch size of 18 (across 6 Volta V100 GPUs) with the Adam optimizer using a learning rate of $2E-4$. The soft constrained model uses a residue penalty factor of 0.01.

E ADDITIONAL VISUALIZATION

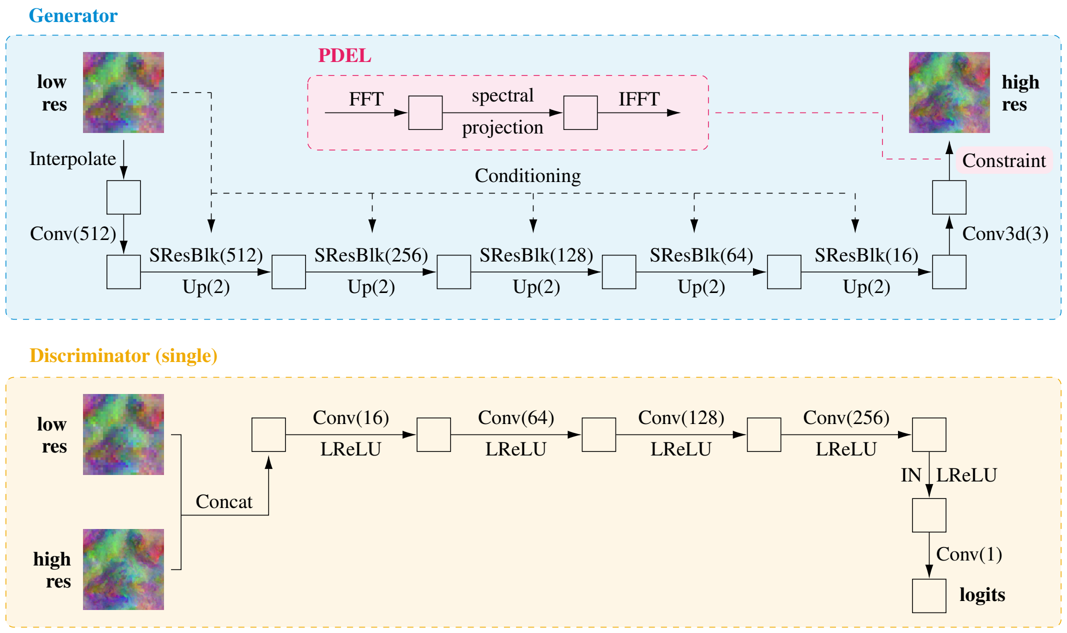

Figure 3: Schematic for the network architecture for the turbulent flow superresolution task. The network is a modified GauGAN (Park et al. (2019)) architecture for 3D fields that utilizes spatially-adaptive normalization for conditioning with the input, and residual blocks for facilitating gradient flows. The network inputs a low resolution flow field in $\mathbb{R}^{32\times32\times32}$ and outputs an output field of $\mathbb{R}^{128\times128\times128}$ with an upscaling factor of 4 in each dimension.

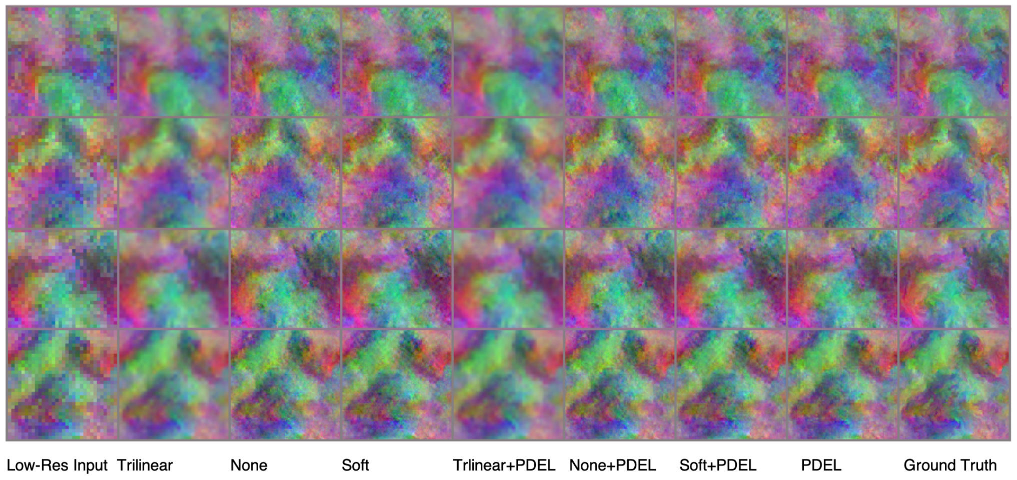

Figure 4: Visualizations for low resolution inputs from the test set, predictions by various models, along with the ground truth flow fields. The flow fields are colored by mapping the three velocity components to RGB channels respectively. The 2d images are slice plots in the z dimension.